

Machine Learning Framework for Characterizing Processing–Structure Relationship in Block Copolymer Thin Films

Bradley Lamb,^{†,||} Saroj Upreti,^{†,||} Yunfei Wang,[†] Daniel Struble,[†] Chenhui
Zhu,[‡] Guillaume Freychet,[¶] Xiaodan Gu,^{*,†} and Boran Ma^{*,†}

[†]*School of Polymer Science and Engineering, University of Southern Mississippi, 118 College
Drive, Hattiesburg, MS 39406, USA*

[‡]*Advanced Light Source, Lawrence Berkeley National Laboratory, Berkeley, CA 94720, USA*

[¶]*NSLS-II, Brookhaven National Laboratory, Upton, New York 11973, USA*

[§]*University of Grenoble Alpes, CEA, Leti, Grenoble, F-38000 France*

||These authors contributed equally to this work

E-mail: xiaodan.gu@usm.edu; boran.ma@usm.edu

Abstract

The morphology of block copolymers (BCPs) critically influences material properties and applications. This work introduces a machine learning (ML)-enabled, high-throughput framework for analyzing grazing incidence small-angle X-ray scattering (GISAXS) data and atomic force microscopy (AFM) images to characterize BCP thin film morphology. A convolutional neural network was trained to classify AFM images by morphology type, achieving 97% testing accuracy. Classified images were then analyzed to extract 2D grain size measurements from the samples in a high-throughput manner. ML models were developed to predict morphological features based on processing parameters such as solvent ratio, additive type, and

additive ratio. GISAXS-based properties were predicted with strong performances ($R^2 > 0.75$), while AFM-based property predictions were less accurate ($R^2 < 0.60$), likely due to the localized nature of AFM measurements compared to the bulk information captured by GISAXS. Beyond model performance, interpretability was addressed using Shapley Additive exPlanations (SHAP). SHAP analysis revealed that the additive ratio had the largest impact on morphological predictions, where additive provides the BCP chains with increased volume to rearrange into thermodynamically favorable morphologies. This interpretability helps validate model predictions and offers insight into parameter importance. Altogether, the presented framework combining high-throughput characterization and interpretable ML offers an approach to exploring and optimizing BCP thin film morphology across a broad processing landscape.

Keywords

Block Copolymer Thin Films, Processing, Morphology, High-Throughput Experimentation, Machine learning, Interpretable Machine Learning

Introduction

Copolymer thin films consist of a wide range of materials with a vast array of applications spanning from membrane technologies for gas separation to energy applications including solid electrolytes.¹⁻³ They exhibit a diverse range of tunable properties dependent on both chemical structure and morphology. Copolymers, specifically block copolymers (BCPs), are a class of polymers in which multiple chemically distinct polymer chains, as building blocks, are bonded together forming one macromolecule. When the blocks of a copolymer are immiscible, unfavorable interactions between the blocks lead to phase separation resulting in unique morphologies.⁴ These unique nanoscale phase-separated microdomains can be leveraged to facilitate the design of advanced materials.^{5,6} For example, BCP membranes find higher applicability compared to traditional inorganic membrane materials in water purification, battery electrolytes, and gas separation fields.⁷

BCP self-assembly behavior at thermodynamic equilibrium can be accurately predicted using self-consistent field theory.⁸⁻¹⁰ The theory-predicted morphology of BCPs is primarily dictated by interactions between the blocks, known as the Flory-Huggins interaction parameter χ , the degree of polymerization N , and the volume fraction of each block ϕ .¹¹ In solid state, the phase diagram can be more complex due to polymer chains becoming kinetically trapped during sample preparation, resulting in a non-equilibrium state. Additionally, interfacial energies and confinement effects further increase the complexity of BCP self-assembly behavior.¹²⁻¹⁴

To achieve precise control over BCP solid state morphology, processing conditions such as solvent type, sample casting method, and post-deposition annealing technique require optimization.¹⁵ The importance of solvent type is especially pronounced when the solvent is selective toward a specific block. In this case, changing the selectivity of the solvent may result in changes in the BCP morphology.¹⁶ Additionally, annealing techniques such as thermal and solvent-vapor annealing of BCP thin films play a large role in the final morphology. These techniques allow for increased mobility of the polymer chains, leading to a more thermodynamically favorable morphology.⁷ Moreover, casting methods such as drop casting and spin coating of BCP solution also affect the morphology mainly due to variation in solvent evaporation dynamics. Spin coating promotes rapid solvent removal and shear induced alignment resulting in uniform films with well-ordered microdomains and reduced defect densities.^{17,18} On the other hand, slower solvent evaporation during drop casting leads to thicker films with varied domain orientation and rougher surface features.¹⁷⁻¹⁹ Therefore, these differences affect overall phase behavior and domain spacing, as the interplay between solvent evaporation, interfacial energetics, and film thickness determine the degree of phase separation and ordering.¹⁹⁻²¹

Scattering and microscopy are common techniques for morphological characterization of BCP films. Grazing incidence small-angle X-ray scattering (GISAXS) is an inverse-space characterization technique measuring the phase behavior of BCP films to extract the average domain spacing and degree of ordering, where the domain of a BCP refers to the aggregation of a specific block.²² Atomic force microscopy (AFM) is a real-space characterization technique that can pro-

vide insights in BCP surface morphology and serve as a complementary characterization method to GISAXS.²³ Moreover, periodically ordered arrangements of BCP domains, i.e., grains, can be identified and measured in AFM as well. However, analysis of characterization data of BCPs remains time-consuming, as manual analysis is often required, especially for features such as grain size from AFM images.

Despite yielding great achievements, the traditional process of BCP solid state morphology control is constrained by laborious experimentation and data analysis required from researchers for the optimization of processing conditions. High-throughput data analysis and machine learning (ML) algorithms have demonstrated promising results in the field of materials science, offering effective approaches for solving optimization problems.^{24–26} However, these algorithms typically require large datasets for the training process. Due to the complexity of polymer systems, such as their intricate chemical structures, the availability of specific polymer datasets is limited, necessitating high-throughput experiments to generate the required data.^{27–30} Therefore, high-throughput data acquisition, combined with ML-aided data analysis and interpretation, can be leveraged to explore the processing parameter space for controlling the solid-state morphology of BCPs.

ML algorithms are extremely diverse, tailored for specific tasks and datasets. These algorithms seek to identify relationships within a labeled training dataset, in the case of supervised learning, optimizing the performance metric.³¹ Within supervised learning, there are two primary tasks: regression and classification. The key difference between these two tasks is the output: a numerical value for regression and a categorical output for classification.³² In the field of materials science, these models have provided researchers with an approach to reducing experimentation by predicting the properties of untested systems, as well as a tool to understand the relationships within complex material systems.^{33–36} Numerous models have been applied in the materials science field to great success, ranging from random forest (RF), support vector machine (SVM), multilayer perceptron (MLP), and extreme gradient boosting (XGB).^{37–44} Within the polymer field, ML has been leveraged to decipher scattering profiles and AFM images of polymers, elucidating polymer conformational and morphological features.^{45–48} Specifically, the Jayaraman group has pioneered

the integration of ML and molecular simulations to advance the interpretation of scattering data from complex polymer solutions. Their approach enables the analysis of scattering profiles that lack conventional fitting equations, overcoming a major limitation in characterizing novel polymer architectures. These works significantly broaden the applicability of scattering experiments, offering new insights into the structure and behavior of emerging polymer systems.^{49–51}

Despite the widespread use of ML for polymer property predictions in the solution and solid state, comparatively little work has focused on the utilization of ML to understand how processing conditions influence the solid-state morphology of BCPs – an area critical for the design of functional materials. Furthermore, generating large datasets in the field of polymer science remains a significant challenge due to long experimentation and analysis times. Many studies have circumvented this issue by compiling pre-existing data from online databases and published papers into a single dataset.^{24,52–54} However, this compiled data can be highly variable, as it comes from different laboratories, leading to inconsistencies in both the experimental setups and data analysis, as well as missed or mislabeled descriptors.

Therefore, the synergistic use of high-throughput data analysis and ML methods can address the previously mentioned challenges and accelerate the rational design of polymeric materials.⁵⁵ In this paper, we present an approach for the high-throughput data analysis of BCP thin film GISAXS profiles and two-dimensional grain sizes measured by AFM, creating a robust dataset of morphological properties from over 200 BCP thin films. In addition, interpretable ML is leveraged to evaluate the relationship between processing parameters and BCP morphology, and offers direct morphological property predictions from processing conditions. This work serves as a proof of concept for an integrated high-throughput data analysis-ML framework for the optimization of processing conditions for polymeric materials (Fig. 1).

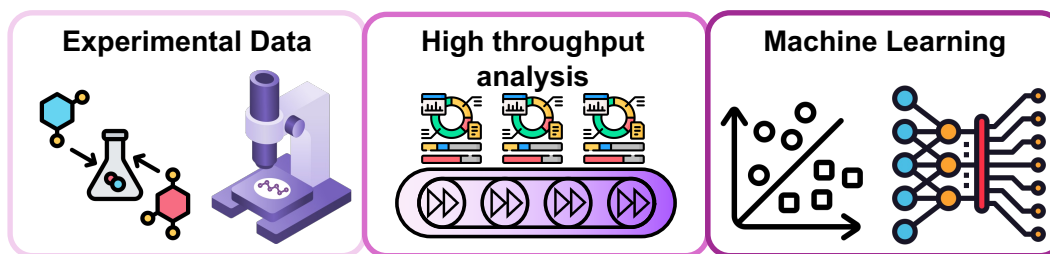


Figure 1: Process flow for the high-throughput analysis of experimentally collected data, curated for machine learning applications and property predictions.

Methodology

Experimentation and characterization

Polystyrene-block-poly (ethylene oxide) (PS-*b*-PEO) ($M_n = 23\text{-}b\text{-}7$ kg/mol) was used as a model system to generate thin films using the “nonvolatile additive solvent annealing” (NVASA) approach. The details of the NVASA process can be found in our previous publication.⁵⁶ PS-*b*-PEO was dissolved overnight in host solvents composed of mixtures of toluene and tetrahydrofuran (THF) at the following volume ratios, 100:0, 90:10, 80:20, 70:30, 60:40 and 50:50, to form 2 to 3 wt% stock solutions. With NVASA, it has been previously reported that a controlled amount of high boiling point additive can briefly remain in the polymer films after the primary low boiling point solvent evaporates after spin coating, thereby swelling the BCP thin film, providing segmental mobility and improving domain order.⁵⁷ Therefore, for each stock solution, varied masses of a high boiling point additive: chloronaphthalene (CN), or methylnaphthalene (MN), were added to achieve additive ratios from 1.00 to 7.00. The control of additive ratio is dictated by the mass of additive relative to the mass of BCP (Equation 1).

$$\text{Additive Ratio} = \frac{\text{mass}_{\text{additive}}}{\text{mass}_{\text{BCP}}} + 1 \quad (1)$$

For instance, an additive ratio of 1.00 indicates no additive (therefore no swelling of the BCP film), whereas additive ratios of 2.00, 3.00, and 3.25 equate to 1:1, 2:1, and 2.25:1 mass ratio of additive:BCP, respectively. These solutions were then spin coated at 2000 rpm for 60 s on silicon

wafers after oxygen plasma cleaning for 5 min (Diener Inc. at 10 mTorr, 20 sccm O₂, 40 W). The coated films were dried under ambient conditions. 202 samples were prepared in total.

GISAXS experiments were carried out at beamline 7.3.3 of Advanced Light Source (ALS) at Lawrence Berkeley National Laboratory, and Beamline 12-ID of National Synchrotron Light Source II (NSLS-II) at Brookhaven National Laboratory. The X-ray energies used at the ALS and NSLS-II were 10 keV and 16.1 keV, respectively. The incidence angle between the sample surface and X-rays was 0.14° and 0.12° for ALS and NSLS-II respectively, and the sample-to-detector distance was 3.5 meters and 4 meters at the ALS and NSLS-II, respectively. The scattering profiles were recorded on Pilatus 2M detector (ALS) and a Pilatus 1M detector (NSLS-II). Igor Pro software, equipped with the Nika and Irena packages, was used to process the 2D scattering patterns and extract 1D line profiles, which were subsequently analyzed using a high-throughput approach.

Oxford Cypher Asylum AFM was used to image the surface morphology of BCP thin films. Phase and height images (1 μm \times 1 μm) with resolution of 256 \times 256 pixels were taken in tapping mode. The tapping mode cantilevers (Tap300AI-G) with force constant of 40 N/m and resonant frequency of 300 kHz were used to scan the surface of films at a rate of 1.95 Hz. AFM raw data were collected using Igor Pro-based software, then flattened, and exported as images using Gwyddion software. These images were later processed in high-throughput fashion to extract properties of interest.

High-throughput data analysis

GISAXS

The 1D GISAXS profiles, obtained from horizontal line cuts of the 2D scattering patterns, were analyzed by first identifying and isolating the primary peak, which is related to the characteristic length scale in the sample, or domain spacing. The peak region was then fit to a combination of a

power-law decay and a Gaussian function (Equation 2):

$$I(q) = A + Cq^{-d} + De^{-\frac{4\ln(2)(q-b)^2}{w^2}} \quad (2)$$

In this equation, $I(q)$ represents the scattering intensity as a function of the scattering vector q . The constant A accounts for a baseline background offset, while the term Cq^{-d} models a power law decay commonly associated with background or form factor scattering, with C as the amplitude and d as the decay exponent. The Gaussian peak is characterized by an amplitude D , a center position b , and a full width at half maximum (FWHM) w . The peak position b is used to calculate the domain spacing ds , using the relation $ds = 2\pi/b$. The FWHM, w , reflects the distribution of domain spacings and serves as an indicator of the degree of structural order in the sample. This fitting function enables simultaneous characterization of both periodic structural features and background scattering behavior.⁵⁸ An in-house Python script was used to fit the scattering data, minimizing the sum of squared residuals within 50,000 maximum function evaluations. The script outputs the final fitted values for peak position and FWHM, along with the coefficient of determination (R^2) of the fitted function. This process for GISAXS analysis is both highly accurate and computationally efficient, with an average fitting R^2 of 0.99, taking less than 1 second per sample (Fig. 2).

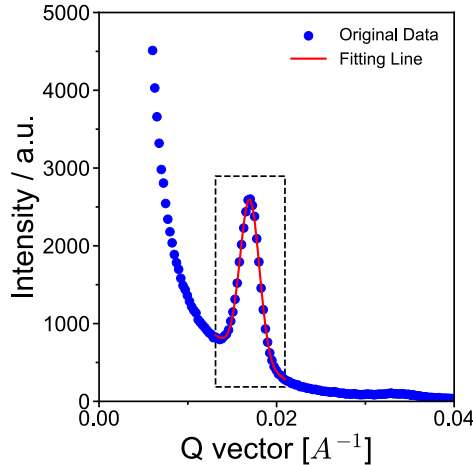


Figure 2: Example peak fitting of 1D GISAXS profile, restricting the fitting functions within the peak region, indicated by the dashed box, to improve fitting of the scattering peak related to the BCP sample.

AFM

The BCP thin films in this study are expected to arrange in hexagonal cylinder morphologies, given the PS-*b*-PEO block ratio. However, the orientation and ordering of the cylinders is highly dependent on the processing conditions of the BCP films.⁵⁹ Therefore, the 202 AFM images collected represent various orientations of hexagonally packed cylinders, including vertical and horizontal alignments, which manifest as ‘dot’- and ‘line’-type features in the AFM images, respectively. While no single approach is sufficient to analyze the local ordering, or grain size, of the microdomains for different alignments, multiple approaches can be used in tandem to create a robust AFM analysis approach (Fig. 3).

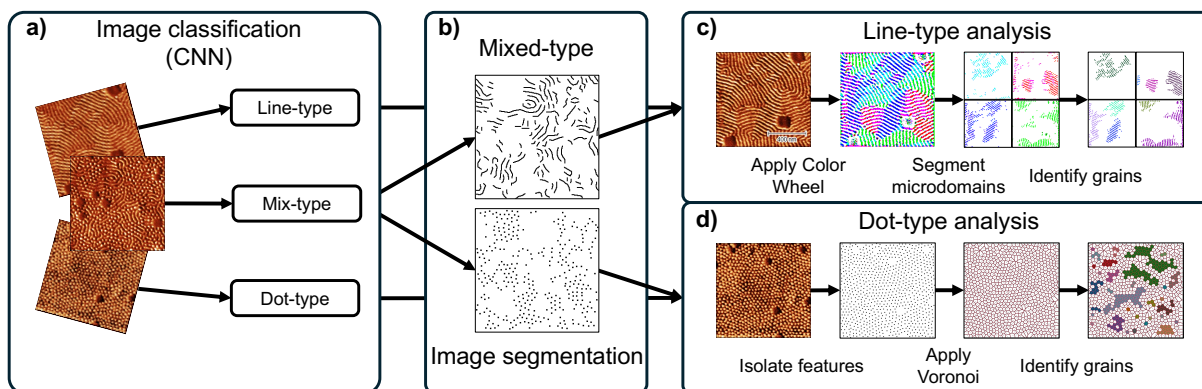


Figure 3: Overview of the high-throughput AFM image analysis process for extracting grain size. a) AFM images are classified based on morphology by a convolutional neural network (CNN). b) Images of mixed-type morphology are segmented into dot- and line-type features. c) Color-wheel analysis of line-type images, color-coding microdomains based on orientation, then segmenting the color-coded microdomains before determining grains. d) Voronoi analysis of dot-type images, features are first isolated before applying the Voronoi analysis and identifying grains.

AFM images are first classified into three categories (Fig. 3 a) depending on the alignment of the hexagonal cylinders with the use of a convolutional neural network (CNN), discussed in more detail in the following section. After classification, the binarized dot- and line-type images were ready for analysis, however, the mixed-type images required further pre-processing. Segmentation of the mixed-type images was performed using the labelme software to create two distinct masks for the dot- and line-type features (Fig. 3 b).⁶⁰ The segmented masks were treated the same as the dot- and line-type images for further analysis.

For line-type images, the MLEExchange color wheel was applied to the Two-dimensional fast Fourier transforms (2D FFT) of the AFM images, which assigns a unique color to the microdomains of different orientations (Fig. 3 c).⁶¹ After isolating one phase from the color wheel image, i.e. filtering out one of the blocks, the microdomains were segmented by creating masks related to each orientation. Once isolated, the scikit-learn cluster package was used to group adjacent pixels together, which were then filtered according to a size threshold to reduce noise in the images.⁶² Individual grains were identified by another clustering analysis before applying another threshold to filter out grains smaller than 150% of the average, again to reduce noise and artificial grains. The final grain size was then calculated by averaging the grain sizes for each sample, then converting from pixels² to μm^2 . In total, this grain analysis process takes approximately 8 seconds per image. Furthermore, the in-house grain analysis code was evaluated, and results were generally in agreement with grain analysis from a separate study⁶³ which is discussed in more detail in the SI.

Separately, the dot-type images were analyzed using Voronoi analysis (Fig. 3 d). Traditionally, Voronoi type analyses are used to identify grain boundaries and defects in well-ordered BCP systems.^{64,65} The following approach, however, leverages the Voronoi analysis to characterize two-dimensional grain sizes for weakly-ordered systems. Within the analysis, the dot-type features were first isolated using the labelme software, creating discrete points for each dot-type feature. Voronoi cells were constructed by treating each feature in the image as a center point. The image was divided such that each cell contains the area closer to its feature than to any other, resulting in a set of perfectly adjacent, non-overlapping regions—one surrounding each dot-like feature. For an ideal hexagonal cylinder morphology, each Voronoi cell should have 6 equal edges, reflecting 6 surrounding hexagonally packed cylinders. Therefore, the numbers of edges for each cell were determined, additionally having to satisfy a criteria being within a 55% threshold of the mode edge length in the image, in order to filter edges at the end of the image or near a defect. Additionally, for a cell to be considered for the grain analysis, the 6 edges must be within 2.5% of each other, ensuring well-ordered hexagonal packing. Finally, adjacent cells were grouped together, and the average grain size determined across all grains for a given sample. The Voronoi analysis occurs

rapidly, taking only 3 seconds per image.

Additionally, local domain spacing measurements were obtained from the AFM images. 2D FFTs were performed on the cleaned and binarized images to obtain the characteristic length scale of the phase-separated microstructure in the BCPs. The radial distribution profile was extracted based on the frequency spectrum in the Fourier space. The radial distribution data was then fit to Equation 2, similar to the GISAXS data fitting, to improve resolution and more accurately determine the peak position than would be possible from the unfitted data alone. The correlation peak from the 2D FFT was then converted using Equation 3 to obtain the characteristic length scale (domain spacing, ds) in real space:

$$ds = \frac{FOV}{u} \quad (3)$$

where u is the peak position of the radial distribution, and FOV is the field of view of the AFM images (i.e. image size, such as $1 \mu\text{m}^2$ for images in Fig. 3).⁶⁶ This process occurs rapidly, taking less than 10 seconds for all 202 samples, while maintaining a high degree of fitting accuracy with an R^2 of 0.96.

Convolutional Neural Network AFM Image Classification

A CNN was first employed to classify the AFM images based on their morphological alignments, specifically, line-, dot-, and mixed-type features, corresponding to vertically aligned cylinders, horizontally aligned hexagonal cylinders, and a combination of both. The CNN was trained using the binarized images as inputs and manually labeled classes as targets. Additionally, due to a significant imbalance of images with line-type morphologies relative to the images with dot- and mixed-type morphologies, the images within the latter classes were augmented, creating three copies of each image rotated in increments of 90° , creating a more balanced dataset. Furthermore, the dot-type images were reflected horizontally and vertically to further increase the amount of data for the class. After augmentation, the dataset was much more balanced, with 171, 84, and 72

images for line-, dot-, and mixed-type morphologies, respectively.

The model follows a simplified VGG-like structure,⁶⁷ consisting of three convolutional blocks with two convolutional layers each, followed by batch normalization, ReLU activations, and max pooling (Fig. 4 a). A more detailed description of the CNN can be found in the SI. Among the 327 AFM images used in the classification task, 228 were allocated for training, 65 for validation, and 34 for testing. On the test set, the CNN model achieved a high classification accuracy of 97.06%. To interpret the model’s decision-making process, the Shapley Additive exPlanations (SHAP) Python package was employed (Fig. 4 b-d). SHAP analysis provides a unified framework for explaining ML model predictions by assigning each feature an importance value—its SHAP value—based on its contribution to the model’s output.⁶⁸

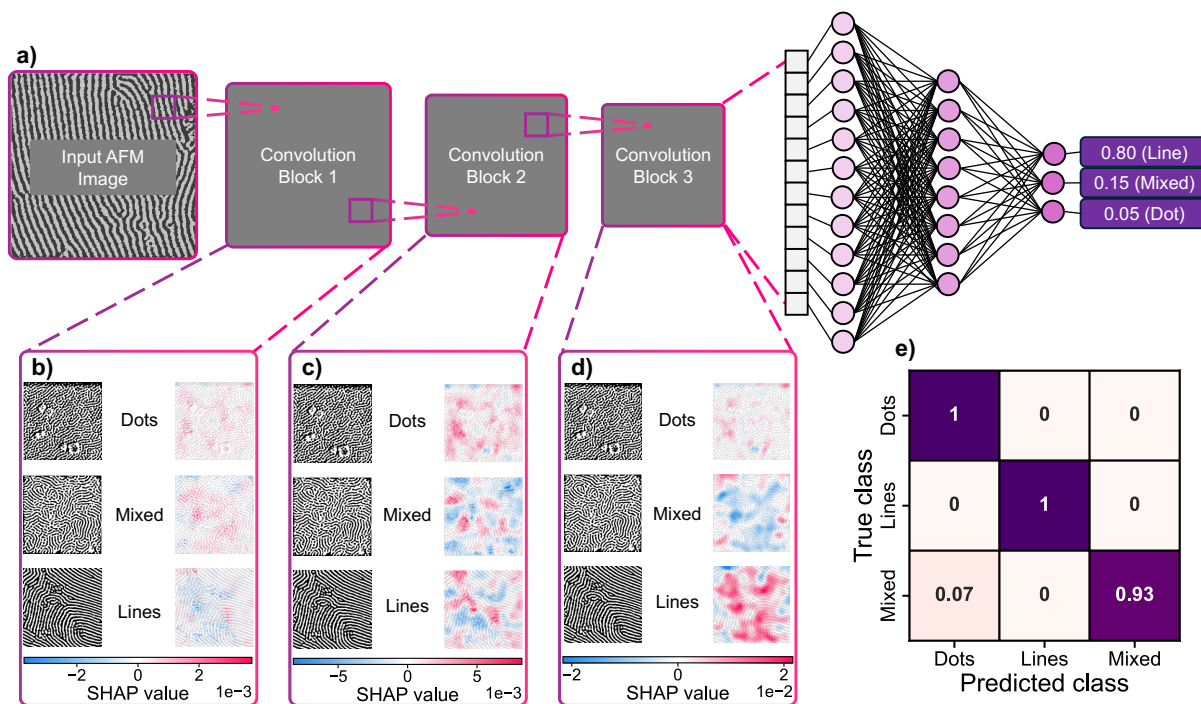


Figure 4: a) Simplified architecture of the CNN used for morphological classification. AFM images are passed through a series of convolutional blocks to extract hierarchical feature maps, which are then fed into fully connected layers to produce a probabilistic prediction over the three morphological classes (line, dot, and mixed). b-d) SHAP-based interpretation of the CNN’s predictions at convolutional block 1-3. Positive SHAP values (red) highlight features that positively contribute to the predicted class, while negative SHAP values (blue) indicate features that negatively influence the prediction. e) Confusion matrix summarizing the CNN’s performance on the test set.

Within each convolutional block, features were extracted from the input to generate feature

maps. After each block, spatial dimensions were reduced, causing fine-scale features to be captured in the earlier blocks, while progressively larger and more abstract features were analyzed in subsequent blocks. The SHAP analysis of block 1 reveals that features evaluated at smaller length scales exhibit strong positive correlations with dot- and mixed-type morphologies, such as dots and disconnections in the line features. This aligns with the physical interpretation of the images, where these morphologies characteristically lack prominent larger structural features. Similarly, the SHAP analysis of block 2 reveals positive correlation between clusters of dots with the dot-type morphology, and groups and lines with heavy curvature with the mixed-type morphologies. Interestingly, block 2 also begins to pick up parallel groups of line features, positively correlating them with the line-type morphology. Finally, features extracted from block 3 primarily correlate positively with the line-type morphology, focusing on long stretches of line features. Overall, the CNN performed exceptionally well distinguishing between dot- and line-type morphologies, however, struggled with the mixed-type morphologies, over-predicting the dot-type morphology for some mixed-type images (Fig. 4 e).

Results and Discussion

Dataset overview

As mentioned previously, the processing parameters explored in this study include solvent ratios of toluene:THF from 0.5 to 1.0, additive ratios from 1.00 to 7.00, and additive types of CN and MN. Domain spacing and FWHM from GISAXS measurements show narrow distributions, with domain spacing measurements around 36 nm and FWHM around 0.0025 \AA^{-1} (Fig. 5 a, b). These distributions indicate the majority of the BCP films have relatively good ordering, indicated by the low FWHM value which is reflective of a narrow distribution of domain spacings in the sample. However, the AFM-measured morphological properties, domain spacing and grain size, demonstrate broader distributions (Fig. 5 c, d). While the range of values for the GISAXS and AFM-based measurements are in agreement with each other, the localized nature of the AFM measurements

effects introduced by the additive, such as differential evaporation dynamics, not captured by bulk GISAXS measurements. In the case of GISAXS-measured FWHM, the correlation may reflect broader distributions of domain spacings within the sample, suggesting increased structural heterogeneity without significantly altering the average domain spacing. Meanwhile, solvent ratio has a relatively low Pearson correlation across all measured outputs. Although solvent plays a critical role in the initial solubilization of the polymers, it has little effect on the resulting morphology of the BCP film, due to the low boiling point solvent volatilizing during the spin coating process. Furthermore, the Pearson correlations were evaluated for the morphological outputs with respect to each other (Fig. 5 f). The domain spacing from both GISAXS and AFM has a fairly large Pearson correlation, indicating good agreement between the measurements from the two approaches. Domain spacing from GISAXS and AFM are inversely correlated with GISAXS-measured FWHM, indicating that as the samples become more ordered, i.e., decreasing FWHM, domain spacing increases. Additionally, the grain size has positive Pearson correlations with domain spacing and an inverse correlation with FWHM, again indicating that as the samples become more ordered, the grain size increases. Scatter plots of the morphological properties are shown in the SI.

Processing–structure classification

Processing condition-trained model

Classification models were trained using solvent ratio, additive ratio, and additive type as input features, with manually labeled ‘weakly-ordered’ and ‘well-ordered’ morphologies - based on AFM images - as the target output. Support Vector Classifier (SVC) and Random Forest Classifier (RFC) were selected for this task due to their robust performance and high accuracy in classification problems. The data set was split using 80% as the training set, and 20% for the test set to evaluate the model performance while using a 5-fold cross validation to ensure generalizability. A grid search approach was employed to evaluate various combinations of hyperparameters, which can be found in the SI for each model. The PyTorch accuracy metric was used to evaluate the models, in which the model with the best cross-validation accuracy was selected.

Both classifiers performed exceedingly well, with RFC performing slightly better than SVC, with cross-validation accuracies of 0.98 and 0.95, respectively. Notably, the RFC model over-predicted the ‘well-ordered’ class, likely due to the class imbalance, with the majority of data falling within the ‘well-ordered’ category (Fig. 6 a). Given the prevalence of SVC in classification tasks, the results were initially surprising. However, due to the relatively small amount of data, RFC was likely able to effectively map the classification task through a series of decision trees, resulting in only three incorrect classifications at the boundary (Fig. 6 b). Therefore, with a relatively small dataset RFC is highly capable of classification tasks, however, SVC could outperform RFC as the dataset increases in both size and complexity.

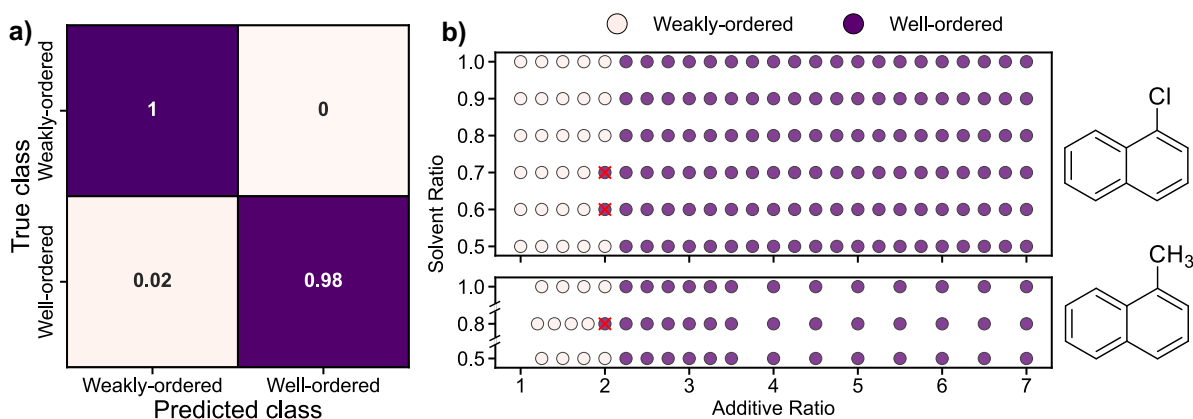


Figure 6: a) Confusion matrix showing the testing results of the RFC model. b) Classification plots illustrating the transition from ‘weakly-ordered’ to ‘well-ordered’ samples as a function of solvent and additive ratios. The plots are separated into two panels: top for the use of CN as the additive and bottom for the use of MN as the additive. Incorrect predictions by the RFC are marked with a red ‘x’.

AFM image-trained model

Further utilizing the AFM images, an additional CNN was trained using the binarized images as inputs and the manually labeled classes of ‘weakly-ordered’ and ‘well-ordered’ as outputs. Additionally, due to an imbalance of well-ordered to weakly-ordered images, 161 and 40 respectively, the images within the weakly-ordered class were augmented, creating three copies of each image rotated in increments of 90 °, creating a more balanced dataset. The CNN utilizes the same custom

framework used to categorize the AFM images based on morphology. The CNN demonstrated similar performance to the previous model, with a testing accuracy of 96%. The model’s predictions were further evaluated using SHAP analysis (Fig. 7).⁶⁸ Similar to the previous CNN, smaller features were identified at early convolutional blocks, building to larger features in subsequent blocks. In this case, the features extracted from blocks 1 and 2 were strongly correlated to the ‘weakly-ordered’ images, such as short, curved lines and dots (Fig. 7 a, b). However, features in block 3 were primarily correlated to the ‘well-ordered’ images, highlighting parallel groups of lines with minimal curvature (Fig. 7 c). Although the dataset was augmented to balance the ‘weakly-ordered’ class, the model still slightly over-predicted for the ‘well-ordered’ class (Fig. 7 d), similar to the RFC model discussed previously.

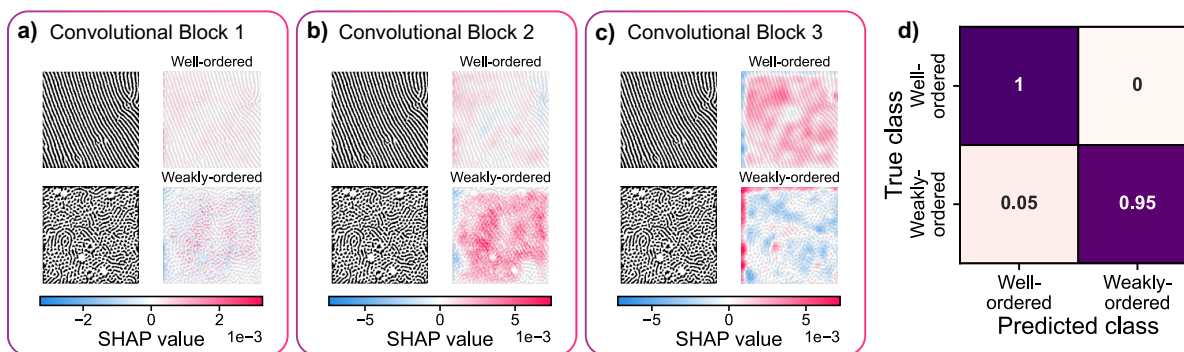


Figure 7: SHAP explanations of predictions at convolutional blocks a) 1, b) 2, and c) 3. Positive SHAP values (red) indicate a positive correlation between the highlighted feature and the predicted output, while negative SHAP values (blue) indicate a negative correlation. d) Confusion matrix showing the CNN’s testing performance.

Processing-structure relationship prediction

Four traditional ML models, including RF, SVM, MLP, and XGB, were trained on the dataset to predict specific morphological properties of the BCP films as a function of the processing conditions. Training was performed with a 5-fold cross-validation and grid-search, using 80% of the data for training and 20% for testing. The set of hyperparameters evaluated within the grid-search can be found in the SI. The evaluation metric used was the coefficient of determination (R^2) in

which the model with the best average cross-validation R^2 was chosen to ensure generalizability (Fig. 8).

RF performed the best for predicting GISAXS-measured domain spacing, achieving a testing R^2 of 0.80, with the majority of prediction errors falling within $\pm 2.5\%$ (Fig. 8 a). The relatively high accuracy is expected given the low variability and narrow distribution of the domain spacing data measured by GISAXS. However, the model performs much better in the high domain spacing region, around 36nm, where the majority of the data is located, than in the low domain spacing region where data is much more sparse. Similarly, RF outperformed the other models when predicting the FWHM with a testing R^2 of 0.75 with the majority of error falling within $\pm 25\%$ (Fig. 8 b). The model performs exceptionally well when predicting FWHM within the ‘narrow-FWHM’ regime, around 0.0025 \AA^{-1} , but struggled with predictions in the ‘broad-FWHM’ region, where data was not as available. Despite the strong correlation and general agreement between the GISAXS and AFM domain spacing measurements, the models trained on domain spacing measured by AFM did not perform as well compared to the models trained on domain spacing measured by GISAXS. XGB performed the best with a testing R^2 of 0.54, with the majority of error distributed within $\pm 5\%$ (Fig. 8 c). Despite the better distribution of data relative to the GISAXS-measured domain spacing, the high variability of the data likely affected the model’s ability to accurately predict the measurements. Interestingly, SVM was the best performing model for predicting the grain size with a testing R^2 of 0.32, but with a much more significant error spread than the previous models (Fig. 8 d). The relatively poor accuracy is again likely due to the local nature of the AFM measurements being highly variable across a given sample. Overall, models trained to predict GISAXS-measured properties outperformed those trained on AFM-measured properties, likely because GISAXS captures bulk characteristics, while AFM probes more localized surface features, leading to increased variability within the data. Additional results from the models can be found in the SI.

The RF models trained on GISAXS-measured domain spacing and FWHM were further evaluated with SHAP given their relatively high degree of accuracy to interpret the model’s predictions

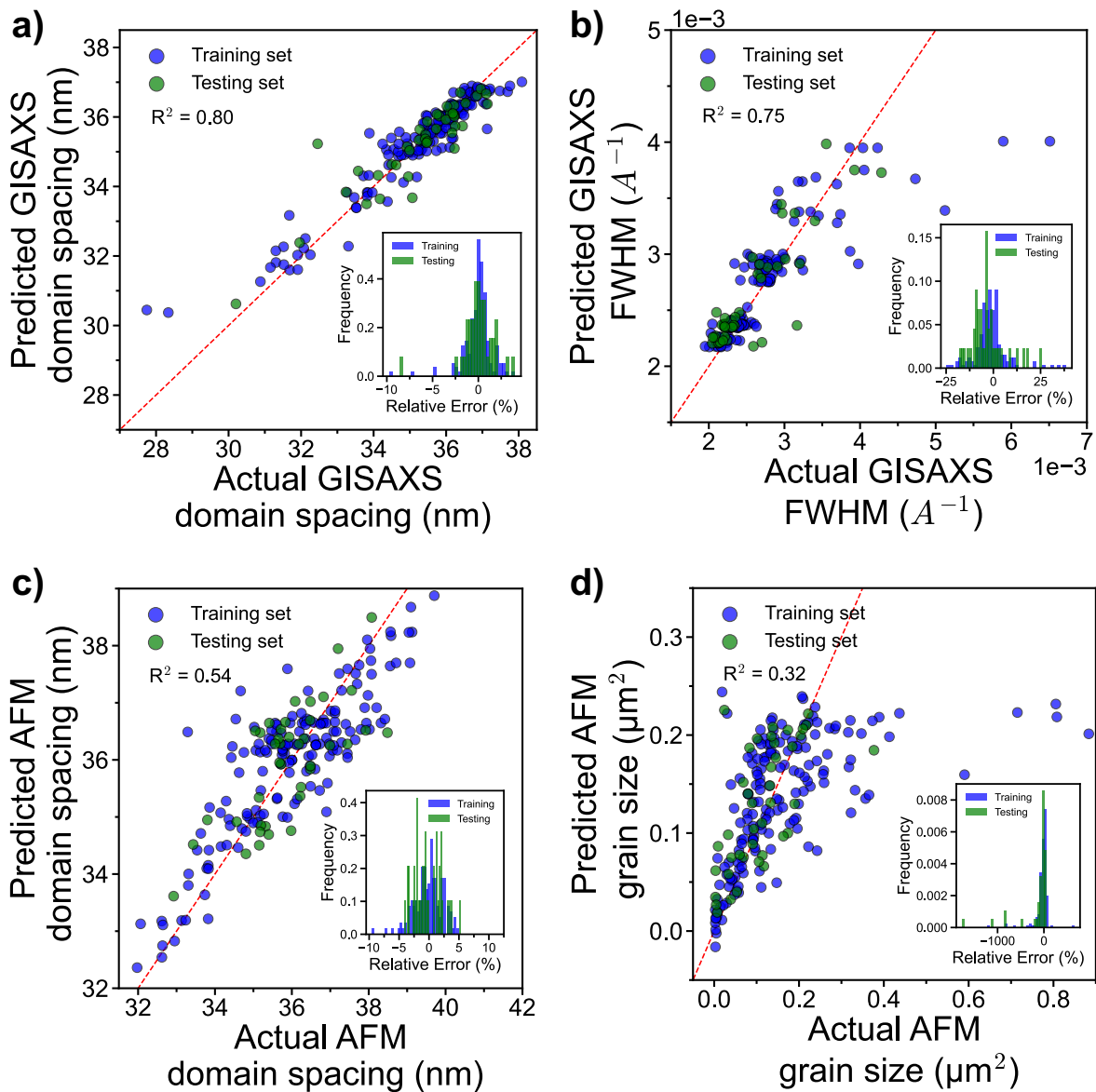


Figure 8: Parity plots with relative error insets for regression model predictions: a) GISAXS-measured domain spacing and b) FWHM predicted by the RF models, and c) AFM-measured domain spacing and d) grain size predicted by the MLP and SVM models respectively.

and evaluate feature importance.⁷⁰ The mean SHAP value for each processing parameter reflects its overall influence on the model's predictions. Meanwhile, local SHAP values reflect the influence of a given parameter on the model's prediction on a per sample basis. In this case, a positive SHAP value indicates that the feature tends to increase the predicted outcome relative to the average prediction. Conversely, a negative SHAP value suggests that the feature generally lowers the prediction relative to the average.

For the RF model trained on GISAXS-measured domain spacing data, additive ratio has a much larger mean SHAP value, 0.95, than solvent ratio, 0.29, and additive type, 0.17 (Fig. 9 a left). This indicates that across all samples, additive ratio has a nearly 3 times greater influence on the resulting BCP domain spacing than the other processing parameters. This is because that the low-volatility additive extends the window for the BCP to rearrange into thermodynamically favorable morphologies, which otherwise remain kinetically trapped. Due to the relatively higher volatility of the solvents, their effects on domain spacing are marginal relative to additive ratio, which is reflected by the substantially lower mean SHAP values. Interestingly, despite small changes in volatility between the additives, the additive type has only a minor overall influence on the predictions, as indicated by its low mean SHAP value.

Moreover, analysis of the local SHAP values for each feature provides a more detailed view of how the processing parameters influence domain spacing predictions on a per-sample basis. Low values of additive ratio (represented by blue dots) have a large spread of SHAP values while higher values of additive ratio (red dots) aggregate around a central SHAP value (Fig. 9 a right). This suggests that domain spacing predictions are more sensitive to changes at lower additive ratios, with the influence tapering off as the additive ratio increases. Although the SHAP values for solvent ratio generally cluster around zero, higher solvent ratios, corresponding to increased toluene content, tend to have a negative impact on the domain spacing predictions, leading to smaller predicted values. This indicates that, although the solvents volatilize during spin coating, the processing history from the solvents have some effects on the final domain spacing of the BCP films. The SHAP values for additive type 0 (CN) are tightly clustered below zero, indicating that

this additive type has a minimal and consistent influence on domain spacing, with little variability across samples. However, for additive type 1 (MN) the SHAP values are much more dispersed, reflecting greater variability in domain spacing when using MN relative to CN.

Furthermore, the local SHAP values were plotted with respect to processing conditions to identify potential cross-relationships between the parameters (Fig. 9 b, c). At low additive ratios, low values of solvent ratio generally lead to slightly higher predicted domain spacing, corresponding to well-ordered samples (Fig. 9 b). This suggests co-solvent systems, solubilizing each segment of the BCP result in better ordered BCP morphologies at low additive ratios. Additionally, as shown in Fig. 9 c, the SHAP values for additive type reveal that the influence of CN on predictions of domain spacing are narrowly aggregated, indicating CN provides good control over BCP morphology. On the other hand, the SHAP values for MN are much more dispersed, and slightly larger than those for CN. Given the slight increase in volatility of MN relative to CN, the increased mobility of the chains does not last as long for MN, therefore kinetically trapping the BCP chains in potentially unfavorable arrangements, leading to more variable, unpredictable domain spacings.

While the SHAP evaluations for the GISAXS-measured FWHM and domain spacing models share some similarities, key differences also emerge. Interestingly, the additive type has a much more significant mean SHAP value for the FWHM predictions, indicating the additive type has a more profound impact on BCP FWHM than domain spacing (Fig. 10 a left). However, additive ratio still maintains the largest mean SHAP value, 0.00029, followed by additive type, 0.00018, and solvent ratio, 0.000054. Similar to the local SHAP analysis for domain spacing, high additive ratios cluster at lower SHAP values, reflecting rapid ordering of the BCP, whereas lower additive ratios exhibit larger and more scattered SHAP values, indicative of weakly-ordered samples with broad FWHM. (Fig. 10 a right). Although the SHAP values for additive type show a similar trend for those related to the domain spacing model, they are far more distinctly separated in the FWHM model, indicating substantial variation in FWHM with changes of additive type. Diving deeper into the SHAP analysis for the FWHM prediction, an interesting relationship can be observed between solvent ratio and additive ratio (Fig. 10 b). Similarly to the trend observed in the domain

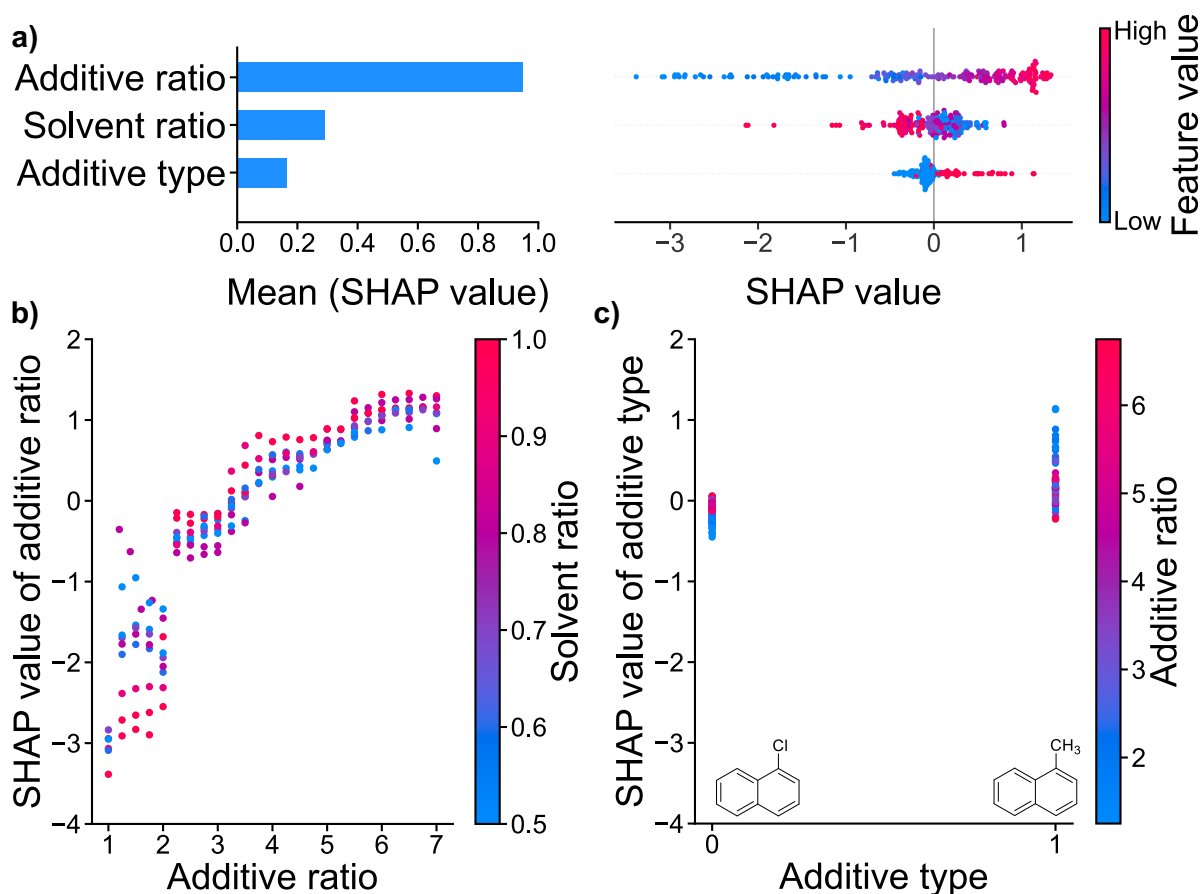


Figure 9: SHAP plots from RFR model trained on GISAXS-measured domain spacing. a) Left: bar chart of the mean SHAP value. Right: beeswarm plots of SHAP value corresponding to individual data points where the dots position on the x-axis indicates the influence of the feature on the model's prediction for the given data point. SHAP dependence plots of b) additive ratio and solvent ratio and c) additive type and additive ratio.

spacing model (Fig. 9 b) but more pronounced, low solvent ratios, reflecting a mixture of toluene and THF, are associated with lower FWHM predictions at low additive ratios, indicating improved ordering from the co-solvents improving the mobility of both blocks in the BCP solution. However, at higher additive ratios, i.e., greater than 2, the relationship reverses and lower solvent ratios contribute to higher FWHM predictions. This suggests a complex relationship between the solvent processing history, the additive ratio, and the FWHM of the BCP films. Additionally, when plotting the SHAP values of additive type against the additive type itself, CN (type 0) shows tightly clustered contributions to FWHM, suggesting consistent and controlled effects on BCP film ordering (Fig. 10 c). In contrast, MN (type 1) is associated with broader and higher FWHM predictions, indicating more variability and poorer control. These results suggest that small changes in volatility of the additive could lead to measurable changes in the ordering of the BCP films.

Conclusion

In summary, a framework enabling the high-throughput analysis of BCP thin film morphology was developed, facilitating analysis of GISAXS and AFM characterization data. The process for extracting domain spacing from both GISAXS and AFM measurements is both highly accurate, time efficient, and provide higher resolution values than the raw data provides. Average fitting R^2 values of 0.99 and 0.96 were achieved for the GISAXS and AFM data, respectively, taking less than one second per sample. Furthermore, two-dimensional values of grain size were obtained by utilizing the AFM image analysis approach of classification, segmentation, and color-wheel or Voronoi analysis depending on the morphology. The CNN classifier proved to be highly accurate and computational inexpensive, while providing physically accurate predictions reflected by the SHAP analysis. Overall, this provides a platform for the rapid exploration of BCP morphological space by accelerating the rate of morphological analysis for the BCP films.

Additionally, the rapid morphological analysis of the BCP films enabled the creation of a dataset for ML model training. RF models were highly capable of accurately classifying sam-

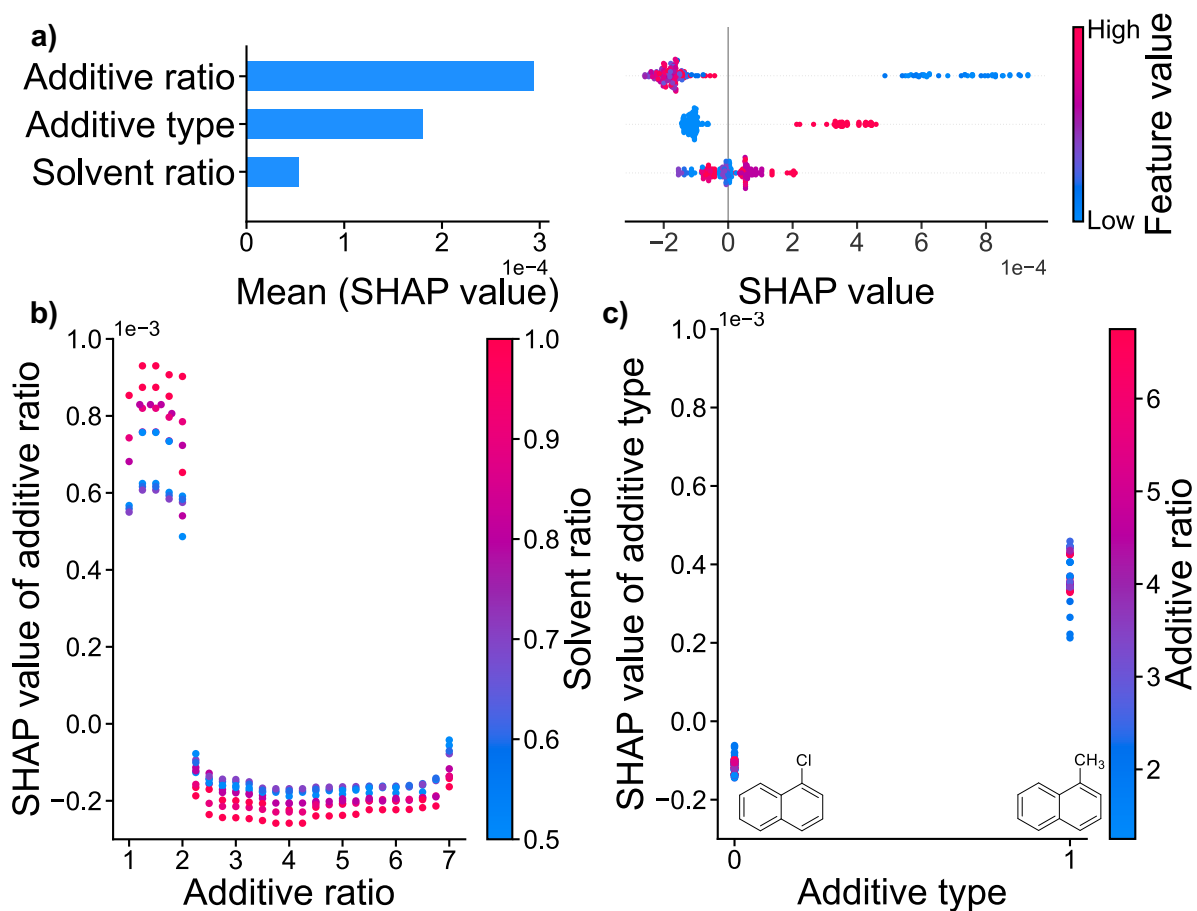


Figure 10: SHAP plots from RFR model trained on GISAXS-measured FWHM. a) Left: bar chart of the mean SHAP value. Right: beeswarm plots of SHAP value corresponding to individual data points where the dots position on the x-axis indicates the influence of the feature on the model's prediction for the given data point. SHAP dependence plots of b) additive ratio and solvent ratio and c) additive type and additive ratio.

ples based on processing conditions, while a CNN achieved similar accuracy using AFM images directly as inputs. The RF models were also extremely accurate when predicting morphological properties measured from GISAXS, however, precision was limited when predicting outside the well-ordered regime due to an imbalance of data. Meanwhile, XGB and SVM models trained on AFM data were generally accurate but their predictive capabilities suffered from variability within the AFM data. SHAP analysis was employed to interpret the processing–structure relationships learned by the RF models from the GISAXS data, confirming that the model’s predictions were physically meaningful. Beyond validating the strong influence of additive ratio, SHAP also revealed interactions between processing history, specifically the solvent ratio and additive ratio, and the GISAXS-measured domain spacing and FWHM. Despite the similar boiling points of the two additives, the slightly lower boiling point of MN resulted in decreased domain spacing, increased FWHM, and more variability among samples relative to those with CN, indicating slight changes in the volatility of the additive have pronounced effects on BCP thin film morphology. The discussed framework combining high-throughput morphological analysis with interpretable ML has demonstrated highly accurate evaluation of BCP thin film morphology. Furthermore, the results not only provided a predictive tool for BCP thin film morphology based on processing conditions, but also a quantitative understanding of the processing–structure relationships.

Future studies could benefit from this approach and focus on expanding the design space to include new polymer chemistries, molecular weights, and different solvent types. Additionally, the variation in AFM data could be greatly improved by collecting multiple replicates across each sample, as well as increasing the field of view of the images. This would not only decrease the variability of the data, but also increase the size of grains able to be measured, allowing for investigation of much more well-ordered samples. Moving forward, these changes should result in significant improvements in the performance of ML models trained on AFM data. However, collection of AFM images is currently one of the largest bottlenecks in this process, requiring significant experimentation time. Increasing both the number of AFM images and the size of the images would further exasperate this bottleneck. Therefore, utilizing a super-resolution approach could

allow for the rapid collection of low-resolution AFM images which could be transformed into high resolution space.⁷¹ With the above-mentioned recommendations in mind, the exploration of BCP thin film morphologies could be greatly accelerated with the use of such an ML-enabled, integrated high-throughput data analysis approach.

Acknowledgement

The authors acknowledge the support from DOE Grant DE-SC0024432. B.M. thanks the Director of the School of Polymer Science and Engineering, the Dean of the College of Arts and Sciences, and the Vice President for Research, all at the University of Southern Mississippi, for their support with generous start-up funds. This research used beamline 7.3.3 of the Advanced Light Source, which is a DOE Office of Science User Facility under contract no. DE-AC02-05CH11231. Y.W. was supported in part by an ALS Doctoral Fellowship in Residence. This research used the Soft Matter Interfaces (SMI) beamline at the National Synchrotron Light Source II, a U.S. DOE Office of Science User Facility operated by Brookhaven National Laboratory under contract no. DE-SC0012704. X.G. thanks NSF for partially supporting his work under the grant no. OIA-2229686.

Data Availability

The dataset and the code used in this study are available at <https://github.com/MaResearchLab/BCP-ML-Characterization-Framework>.

References

- (1) Ghosal, K.; Freeman, B. D. Gas separation using polymer membranes: an overview. *Polymers for Advanced Technologies* **1994**, *5*, 673–697, [_eprint: https://onlinelibrary.wiley.com/doi/pdf/10.1002/pat.1994.220051102](https://onlinelibrary.wiley.com/doi/pdf/10.1002/pat.1994.220051102).

- (2) Mosciatti, T.; del Rosso, M. G.; Herder, M.; Frisch, J.; Koch, N.; Hecht, S.; Orgiu, E.; Samorì, P. Light-Modulation of the Charge Injection in a Polymer Thin-Film Transistor by Functionalizing the Electrodes with Bistable Photochromic Self-Assembled Monolayers. *Advanced Materials* **2016**, *28*, 6606–6611, _eprint: <https://onlinelibrary.wiley.com/doi/pdf/10.1002/adma.201600651>.
- (3) Hou, W.; Xiao, Y.; Han, G.; Lin, J.-Y. The Applications of Polymers in Solar Cells: A Review. *Polymers* **2019**, *11*, 143, Number: 1 Publisher: Multidisciplinary Digital Publishing Institute.
- (4) Darling, S. B. Directing the self-assembly of block copolymers. *Progress in Polymer Science* **2007**, *32*, 1152–1204.
- (5) Heeger, A. J. 25th Anniversary Article: Bulk Heterojunction Solar Cells: Understanding the Mechanism of Operation. *Advanced Materials* **2014**, *26*, 10–28, _eprint: <https://onlinelibrary.wiley.com/doi/pdf/10.1002/adma.201304373>.
- (6) Liu, X.; He, B.; Garzón-Ruiz, A.; Navarro, A.; Chen, T. L.; Kolaczkowski, M. A.; Feng, S.; Zhang, L.; Anderson, C. A.; Chen, J.; Liu, Y. Unraveling the Main Chain and Side Chain Effects on Thin Film Morphology and Charge Transport in Quinoidal Conjugated Polymers. *Advanced Functional Materials* **2018**, *28*, 1801874, _eprint: <https://onlinelibrary.wiley.com/doi/pdf/10.1002/adfm.201801874>.
- (7) Wang, X.-Q.; Wang, T.; Feng, Y.-N.; Zhang, L.-Y.; Zhao, Z.-P. Recent progress on fabrication and applications of advanced block copolymer membranes. *Sustainable Materials and Technologies* **2024**, *39*, e00855.
- (8) Bates, F. S.; Fredrickson, G. H. Block Copolymer Thermodynamics: Theory and Experiment. *Annual Review of Physical Chemistry* **1990**, *41*, 525–557, Publisher: Annual Reviews.
- (9) Helfand, E.; Wasserman, Z. R. Block Copolymer Theory. 4. Narrow Interphase Approximation. *Macromolecules* **1976**, *9*, 879–888, Publisher: American Chemical Society.

- (10) Leibler, L. Theory of Microphase Separation in Block Copolymers. *Macromolecules* **1980**, *13*, 1602–1617, Publisher: American Chemical Society.
- (11) Matsen, M. W.; Bates, F. S. Unifying Weak- and Strong-Segregation Block Copolymer Theories. *Macromolecules* **1996**, *29*, 1091–1098, Publisher: American Chemical Society.
- (12) Mansky, P.; Liu, Y.; Huang, E.; Russell, T. P.; Hawker, C. Controlling Polymer-Surface Interactions with Random Copolymer Brushes. *Science* **1997**, *275*, 1458–1460, Publisher: American Association for the Advancement of Science.
- (13) Han, E.; Stuen, K. O.; Leolukman, M.; Liu, C.-C.; Nealey, P. F.; Gopalan, P. Perpendicular Orientation of Domains in Cylinder-Forming Block Copolymer Thick Films by Controlled Interfacial Interactions. *Macromolecules* **2009**, *42*, 4896–4901, Publisher: American Chemical Society.
- (14) Brassat, K.; Lindner, J. K. N. Nanoscale Block Copolymer Self-Assembly and Microscale Polymer Film Dewetting: Progress in Understanding the Role of Interfacial Energies in the Formation of Hierarchical Nanostructures. *Advanced Materials Interfaces* **2020**, *7*, 1901565, [_eprint: https://onlinelibrary.wiley.com/doi/pdf/10.1002/admi.201901565](https://onlinelibrary.wiley.com/doi/pdf/10.1002/admi.201901565).
- (15) Albalak, R. J.; Thomas, E. L.; Capel, M. S. Thermal annealing of roll-cast triblock copolymer films. *Polymer* **1997**, *38*, 3819–3825.
- (16) Albalak, R. J.; Capel, M. S.; Thomas, E. L. Solvent swelling of roll-cast triblock copolymer films. *Polymer* **1998**, *39*, 1647–1656.
- (17) Zhang, X.; Douglas, J. F.; Jones, R. L. Influence of film casting method on block copolymer ordering in thin films. *Soft Matter* **2012**, *8*, 4980–4987, Publisher: The Royal Society of Chemistry.
- (18) Tyona, M. A theoretical study on spin coating technique. *Advances in materials Research* **2013**, *2*, 195–208.

- (19) Jung, J.; Park, H. W.; Lee, S.; Lee, H.; Chang, T.; Matsunaga, K.; Jinnai, H. Effect of film thickness on the phase behaviors of diblock copolymer thin film. *ACS Nano* **2010**, *4*, 3109–3116, Publisher: American Chemical Society.
- (20) Mishra, V.; Fredrickson, G. H.; Kramer, E. J. Effect of Film Thickness and Domain Spacing on Defect Densities in Directed Self-Assembly of Cylindrical Morphology Block Copolymers. *ACS Nano* **2012**, *6*, 2629–2641, Publisher: American Chemical Society.
- (21) Saito, M.; Ito, K.; Yokoyama, H. Mechanical Properties of Ultrathin Polystyrene-*b*-Polybutadiene-*b*-Polystyrene Block Copolymer Films: Film Thickness-Dependent Young's Modulus. *Macromolecules* **2021**, *54*, 8538–8547, Publisher: American Chemical Society.
- (22) Li, L.; Arras, M. M. L.; Li, T.; Li, W.; Chang, D.; Keum, J. K.; Bonnesen, P. V.; Qian, S.; Peng, X.; Lee, B.; Hong, K. Alternating crystalline lamellar structures from thermodynamically miscible poly(*ε*-caprolactone) H/D blends. *Polymer* **2019**, *175*, 320–328.
- (23) Lorenzoni, M.; Evangelio, L.; Verhaeghe, S.; Nicolet, C.; Navarro, C.; Pérez-Murano, F. Assessing the Local Nanomechanical Properties of Self-Assembled Block Copolymer Thin Films by Peak Force Tapping. *Langmuir* **2015**, *31*, 11630–11638, Publisher: American Chemical Society.
- (24) Struble, D. C.; Lamb, B. G.; Ma, B. A prospective on machine learning challenges, progress, and potential in polymer science. *MRS Communications* **2024**,
- (25) Upadhyaya, R.; Kosuri, S.; Tamasi, M.; Meyer, T. A.; Atta, S.; Webb, M. A.; Gormley, A. J. Automation and data-driven design of polymer therapeutics. *Advanced Drug Delivery Reviews* **2021**, *171*, 1–28.
- (26) MacLeod, B. P. et al. Self-driving laboratory for accelerated discovery of thin-film materials. *Science Advances* **2020**, *6*, eaaz8867, Publisher: American Association for the Advancement of Science.

- (27) Chen, L.; Pilania, G.; Batra, R.; Huan, T. D.; Kim, C.; Kuenneth, C.; Ramprasad, R. Polymer informatics: Current status and critical next steps. *Materials Science and Engineering: R: Reports* **2021**, *144*, 100595.
- (28) Patra, T. K. Data-Driven Methods for Accelerating Polymer Design. *ACS Polymers Au* **2022**, *2*, 8–26, Publisher: American Chemical Society.
- (29) Day, E. C.; Chittari, S. S.; Bogen, M. P.; Knight, A. S. Navigating the Expansive Landscapes of Soft Materials: A User Guide for High-Throughput Workflows. *ACS Polymers Au* **2023**, *3*, 406–427, Publisher: American Chemical Society.
- (30) Schuett, T.; Endres, P.; Standau, T.; Zechel, S.; Albuquerque, R. Q.; Brütting, C.; Ruckdaschel, H.; Schubert, U. S. Application of Digital Methods in Polymer Science and Engineering. *Advanced Functional Materials* **2024**, *34*, 2309844, _eprint: <https://onlinelibrary.wiley.com/doi/pdf/10.1002/adfm.202309844>.
- (31) Jordan, M. I.; Mitchell, T. M. Machine learning: Trends, perspectives, and prospects. *Science* **2015**, *349*, 255–260, Publisher: American Association for the Advancement of Science.
- (32) Castillo-Botón, C.; Casillas-Pérez, D.; Casanova-Mateo, C.; Ghimire, S.; Cerro-Prada, E.; Gutierrez, P. A.; Deo, R. C.; Salcedo-Sanz, S. Machine learning regression and classification methods for fog events prediction. *Atmospheric Research* **2022**, *272*, 106157.
- (33) Wei, J.; Chu, X.; Sun, X.-Y.; Xu, K.; Deng, H.-X.; Chen, J.; Wei, Z.; Lei, M. Machine learning in materials science. *InfoMat* **2019**, *1*, 338–358, _eprint: <https://onlinelibrary.wiley.com/doi/pdf/10.1002/inf2.12028>.
- (34) Ma, B.; Finan, N. J.; Jany, D.; Deagen, M. E.; Schadler, L. S.; Brinson, L. C. Machine-Learning-Assisted Understanding of Polymer Nanocomposites Composition–Property Relationship: A Case Study of NanoMine Database. *Macromolecules* **2023**, *56*, 3945–3953, Publisher: American Chemical Society.

- (35) Lu, S.; Zhou, Q.; Ouyang, Y.; Guo, Y.; Li, Q.; Wang, J. Accelerated discovery of stable lead-free hybrid organic-inorganic perovskites via machine learning. *Nature Communications* **2018**, *9*, 3405, Publisher: Nature Publishing Group.
- (36) Oliynyk, A. O.; Antono, E.; Sparks, T. D.; Ghadbeigi, L.; Gaultois, M. W.; Meredig, B.; Mar, A. High-Throughput Machine-Learning-Driven Synthesis of Full-Heusler Compounds. *Chemistry of Materials* **2016**, *28*, 7324–7331, Publisher: American Chemical Society.
- (37) Fridgeirdottir, G. A.; Harris, R. J.; Dryden, I. L.; Fischer, P. M.; Roberts, C. J. Multiple Linear Regression Modeling To Predict the Stability of Polymer–Drug Solid Dispersions: Comparison of the Effects of Polymers and Manufacturing Methods on Solid Dispersion Stability. *Molecular Pharmaceutics* **2018**, *15*, 1826–1841, Publisher: American Chemical Society.
- (38) Tao, L.; Varshney, V.; Li, Y. Benchmarking Machine Learning Models for Polymer Informatics: An Example of Glass Transition Temperature. *Journal of Chemical Information and Modeling* **2021**, *61*, 5395–5413, Publisher: American Chemical Society.
- (39) Kim, Y.; Oh, H. Comparison between Multiple Regression Analysis, Polynomial Regression Analysis, and an Artificial Neural Network for Tensile Strength Prediction of BFRP and GFRP. *Materials* **2021**, *14*, 4861, Number: 17 Publisher: Multidisciplinary Digital Publishing Institute.
- (40) Banerjee, T.; Samanta, A.; Mandal, A. Mathematical regression models for rheological behavior of interaction between polymer-surfactant binary mixtures and electrolytes. *Journal of Dispersion Science and Technology* **2022**, *43*, 1333–1345, Publisher: Taylor & Francis
_eprint: <https://doi.org/10.1080/01932691.2020.1857261>.
- (41) Liang, J.; Xu, S.; Hu, L.; Zhao, Y.; Zhu, X. Machine-learning-assisted low dielectric constant polymer discovery. *Materials Chemistry Frontiers* **2021**, *5*, 3823–3829, Publisher: The Royal Society of Chemistry.

- (42) Xu, P.; Lu, T.; Ju, L.; Tian, L.; Li, M.; Lu, W. Machine Learning Aided Design of Polymer with Targeted Band Gap Based on DFT Computation. *The Journal of Physical Chemistry B* **2021**, *125*, 601–611, Publisher: American Chemical Society.
- (43) Chen, G.; Tao, L.; Li, Y. Predicting Polymers' Glass Transition Temperature by a Chemical Language Processing Model. *Polymers* **2021**, *13*, 1898, Number: 11 Publisher: Multidisciplinary Digital Publishing Institute.
- (44) Xu, J.; Chen, B.; Liang, H. Accurate Prediction of T_c (Lower Critical Solution Temperature) in Polymer Solutions Based on 3D Descriptors and Artificial Neural Networks. *Macromolecular Theory and Simulations* **2008**, *17*, 109–120, _eprint: <https://onlinelibrary.wiley.com/doi/pdf/10.1002/mats.200700067>.
- (45) Tung, C.-H.; Chang, S.-Y.; Chen, H.-L.; Wang, Y.; Hong, K.; Carrillo, J. M.; Sumpter, B. G.; Shinohara, Y.; Do, C.; Chen, W.-R. Small angle scattering of diblock copolymers profiled by machine learning. *The Journal of Chemical Physics* **2022**, *156*, 131101.
- (46) Ding, L.; Tung, C.-H.; Sumpter, B. G.; Chen, W.-R.; Do, C. Deciphering the Scattering of Mechanically Driven Polymers Using Deep Learning. *Journal of Chemical Theory and Computation* **2025**, *21*, 4176–4182, Publisher: American Chemical Society.
- (47) Kobayashi, Y.; Miyake, Y.; Ishiwari, F.; Ishiwata, S.; Saeki, A. Machine learning of atomic force microscopy images of organic solar cells. *RSC Advances* **2023**, *13*, 15107–15113, Publisher: Royal Society of Chemistry.
- (48) Paruchuri, A.; Wang, Y.; Gu, X.; Jayaraman, A. Machine learning for analyzing atomic force microscopy (AFM) images generated from polymer blends. *Digital Discovery* **2024**, *3*, 2533–2550, Publisher: Royal Society of Chemistry.
- (49) Beltran-Villegas, D. J.; Wessels, M. G.; Lee, J. Y.; Song, Y.; Wooley, K. L.; Pochan, D. J.; Jayaraman, A. Computational Reverse-Engineering Analysis for Scattering Experiments on

- Amphiphilic Block Polymer Solutions. *Journal of the American Chemical Society* **2019**, *141*, 14916–14930.
- (50) Wu, Z.; Jayaraman, A. Machine Learning-Enhanced Computational Reverse-Engineering Analysis for Scattering Experiments (CREASE) for Analyzing Fibrillar Structures in Polymer Solutions. *Macromolecules* **2022**, *55*, 11076–11091.
- (51) Wessels, M. G.; Jayaraman, A. Machine Learning Enhanced Computational Reverse Engineering Analysis for Scattering Experiments (CREASE) to Determine Structures in Amphiphilic Polymer Solutions. *ACS Polymers Au* **2021**, *1*, 153–164, Publisher: American Chemical Society.
- (52) Ethier, J. G.; Casukhela, R. K.; Latimer, J. J.; Jacobsen, M. D.; Rasin, B.; Gupta, M. K.; Baldwin, L. A.; Vaia, R. A. Predicting Phase Behavior of Linear Polymers in Solution Using Machine Learning. *Macromolecules* **2022**, *55*, 2691–2702, Publisher: American Chemical Society.
- (53) Kim, C.; Batra, R.; Chen, L.; Tran, H.; Ramprasad, R. Polymer design using genetic algorithm and machine learning. *Computational Materials Science* **2021**, *186*, 110067.
- (54) Sha, W.; Li, Y.; Tang, S.; Tian, J.; Zhao, Y.; Guo, Y.; Zhang, W.; Zhang, X.; Lu, S.; Cao, Y.-C.; Cheng, S. Machine learning in polymer informatics. *InfoMat* **2021**, *3*, 353–361, _eprint: <https://onlinelibrary.wiley.com/doi/pdf/10.1002/inf2.12167>.
- (55) Eyke, N. S.; Koscher, B. A.; Jensen, K. F. Toward Machine Learning-Enhanced High-Throughput Experimentation. *Trends in Chemistry* **2021**, *3*, 120–132.
- (56) Weller, D. W.; Galuska, L.; Wang, W.; Ehlenburg, D.; Hong, K.; Gu, X. Roll-to-Roll Scalable Production of Ordered Microdomains through Nonvolatile Additive Solvent Annealing of Block Copolymers. *Macromolecules* **2019**, *52*, 5026–5032, Publisher: American Chemical Society.

- (57) Shui, T.-e.; Chang, T.; Wang, Z.; Huang, H. Rapid Assembly of Block Copolymer Thin Films via Accelerating the Swelling Process During Solvent Annealing. *Polymers* **2025**, *17*, 1242, Number: 9 Publisher: Multidisciplinary Digital Publishing Institute.
- (58) Gu, X.; Gunkel, I.; Hexemer, A.; Gu, W.; Russell, T. P. An In Situ Grazing Incidence X-Ray Scattering Study of Block Copolymer Thin Films During Solvent Vapor Annealing. *Advanced Materials* **2014**, *26*, 273–281, _eprint: <https://onlinelibrary.wiley.com/doi/pdf/10.1002/adma.201302562>.
- (59) Hao, J.; Wang, Z.; Wang, Z.; Yin, Y.; Jiang, R.; Li, B.; Wang, Q. Self-Assembly in Block Copolymer Thin Films upon Solvent Evaporation: A Simulation Study. *Macromolecules* **2017**, *50*, 4384–4396, Publisher: American Chemical Society.
- (60) Wada, K. et al. wkentaro/labelme: v4.6.0. 2021; <https://zenodo.org/records/5711226>.
- (61) Zhao, Z. et al. MLExchange: A web-based platform enabling exchangeable machine learning workflows for scientific studies. 2022 4th Annual Workshop on Extreme-scale Experiment-in-the-Loop Computing (XLOOP). 2022; pp 10–15, arXiv:2208.09751 [cs].
- (62) Pedregosa, F. et al. Scikit-learn: Machine Learning in Python. 2018; <http://arxiv.org/abs/1201.0490>, arXiv:1201.0490 [cs].
- (63) Murphy, J. N.; Harris, K. D.; Buriak, J. M. Automated Defect and Correlation Length Analysis of Block Copolymer Thin Film Nanopatterns. *PLOS ONE* **2015**, *10*, e0133088, Publisher: Public Library of Science.
- (64) Hammond, M. R.; Sides, S. W.; Fredrickson, G. H.; Kramer, E. J.; Ruokolainen, J.; Hahn, S. F. Adjustment of Block Copolymer Nanodomain Sizes at Lattice Defect Sites. *Macromolecules* **2003**, *36*, 8712–8716, Publisher: American Chemical Society.

- (65) Bourne, D. P.; Peletier, M. A.; Roper, S. M. Hexagonal Patterns in a Simplified Model for Block Copolymers. *SIAM Journal on Applied Mathematics* **2014**, *74*, 1315–1337, Publisher: Society for Industrial and Applied Mathematics.
- (66) Carmona, P.; Röding, M.; Särkkä, A.; Corswant, C. v.; Olsson, E.; Lorén, N. Structure evolution during phase separation in spin-coated ethylcellulose/hydroxypropylcellulose films. *Soft Matter* **2021**, *17*, 3913–3922, Publisher: The Royal Society of Chemistry.
- (67) Simonyan, K.; Zisserman, A. Very Deep Convolutional Networks for Large-Scale Image Recognition. 2015; <http://arxiv.org/abs/1409.1556>, arXiv:1409.1556 [cs].
- (68) Lundberg, S.; Lee, S.-I. A Unified Approach to Interpreting Model Predictions. 2017; <http://arxiv.org/abs/1705.07874>, arXiv:1705.07874 [cs, stat].
- (69) Ogieglo, W.; Wormeester, H.; Eichhorn, K.-J.; Wessling, M.; Benes, N. E. In situ ellipsometry studies on swelling of thin polymer films: A review. *Progress in Polymer Science* **2015**, *42*, 42–78.
- (70) Lundberg, S. M.; Erion, G.; Chen, H.; DeGrave, A.; Prutkin, J. M.; Nair, B.; Katz, R.; Himelfarb, J.; Bansal, N.; Lee, S.-I. From local explanations to global understanding with explainable AI for trees. *Nature Machine Intelligence* **2020**, *2*, 56–67, Publisher: Nature Publishing Group.
- (71) Chang, M.-C.; Wei, Y.; Chen, W.-R.; Do, C. Accelerating Neutron Scattering Data Collection and Experiments Using AI Deep Super-Resolution Learning. 2019; <http://arxiv.org/abs/1904.08450>, arXiv:1904.08450 [physics].